

In Situ Constructed 3D Lithium Anodes for Long-Cycling All-Solid-State Batteries

Hui Duan, Changhong Wang, Ruizhi Yu, Weihan Li, Jiamin Fu, Xiaofei Yang, Xiaoting Lin, Matthew Zheng, Xiaona Li, Sixu Deng, Xiaoge Hao, Ruying Li, Jiantao Wang,* Huan Huang,* and Xueliang Sun*

Constructing a 3D lithium metal anode has been demonstrated to be the most effective strategy to address its dendrite issue in liquid batteries. However, this promising approach has proved challenging to inherit in all-solid-state Li metal batteries (ASSLMBs) because of the rigidity of inorganic solid electrolytes (SEs), which constrains interfacial solid–solid ionic contact. Herein, a 3D Li anode is in situ constructed for ASSLMBs by spontaneous chemical reactions between halide SEs and Li metal. The in situ formed Li–Al alloys and well-maintained sulfide SEs inside the 3D structure serve as continuous electron and Li^+ transport pathways and facilitate the homogenous distribution of charge carriers. The lithiophilic Li alloy can regulate Li deposition behavior and enable uniform Li nucleation and deposition. Both the Li||Li symmetric and full batteries exhibit good electrochemical performance at high current density. This work provides a universal strategy and new insight perspective to construct 3D Li for high-performance ASSLMBs.

1. Introduction

All-solid-state Li metal batteries (ASSLMBs) are expected to be prominent in safe and dense energy-storage devices.^[1] However, the practical applications of Li metal batteries are severely impeded by Li dendrite formation, interfacial void formation, and considerable interfacial reactions, which lead to battery failure and rapidly deteriorating performance. The Li dendrite growth and interfacial void formation are more serious when cycling at high current densities and large capacities, which is the key hurdle that must be overcome for the practical Li metal anode.^[2] Quite a few strategies, such as exploiting conductive porous materials,^[3] interface modification,^[2b,4] electrode or electrolyte structure design,^[5] and multilayer

solid electrolytes^[6] have been proposed to resolve this challenge in liquid or solid-state batteries. As one of the most efficient approaches, high-surface-area 3D Li metal anodes that can uniformly distribute charge carriers by reducing local current density have been considered a feasible route to prohibit the growth of Li dendrite^[3] and achieved great success in liquid batteries.^[7] However, this strategy is hard to apply in ASSLMBs because of the different natures of liquid electrolytes (LEs) and solid electrolytes (SEs). The fluidity of LEs enables LEs to infiltrate into the microstructures of the 3D Li anode and form a compact interface and interconnected Li^+ transport pathway. However, the solid nature and limited plasticity of the SEs restrict their interfacial ionic contact. SEs also possess insufficient Li^+ transport pathways, because inorganic SEs cannot flow or percolate into the microstructures of 3D Li anode sufficiently.^[1] In addition, some SEs, such as sulfides and halides exhibit poor chemical compatibility with many polar solvents, which greatly limits the application of wet chemical method to infiltrate SEs to the 3D structure.^[8] Therefore, traditional high performing 3D Li anodes used in liquid batteries cannot be simply duplicated in ASSLMBs. Accordingly, to construct a 3D Li anode with sufficient interfacial solid–solid ionic contact and continuous ion transport channels in ASSLMBs remains challenging.

Recently, metal halide SEs with a general formula of Li-M-X (M = trivalent metal, X = F, Cl, Br, I) have attracted significant research attention due to their high ionic conductivity, wide

H. Duan, C. Wang, R. Yu, W. Li, J. Fu, X. Yang, X. Lin, M. Zheng, X. Li, S. Deng, X. Hao, R. Li, X. Sun
Department of Mechanical and Materials Engineering
University of Western Ontario
London, Ontario N6A 5B9, Canada
E-mail: xsun9@uwo.ca

J. Wang
China Automotive Battery Research Institute Co., Ltd
Yanqi Economic Development Area
No. 11 Xingke East Street, Huairou District, Beijing 101407, China
E-mail: wangjt@glabat.com

H. Huang
Glabat Solid-State Battery Inc.
700 Collip Circle, London, Ontario N6G 4X8, Canada
E-mail: hhuang@glabat-ssb.com

 The ORCID identification number(s) for the author(s) of this article can be found under <https://doi.org/10.1002/aenm.202300815>

© 2023 The Authors. Advanced Energy Materials published by Wiley-VCH GmbH. This is an open access article under the terms of the Creative Commons Attribution-NonCommercial-NoDerivs License, which permits use and distribution in any medium, provided the original work is properly cited, the use is non-commercial and no modifications or adaptations are made.

DOI: 10.1002/aenm.202300815

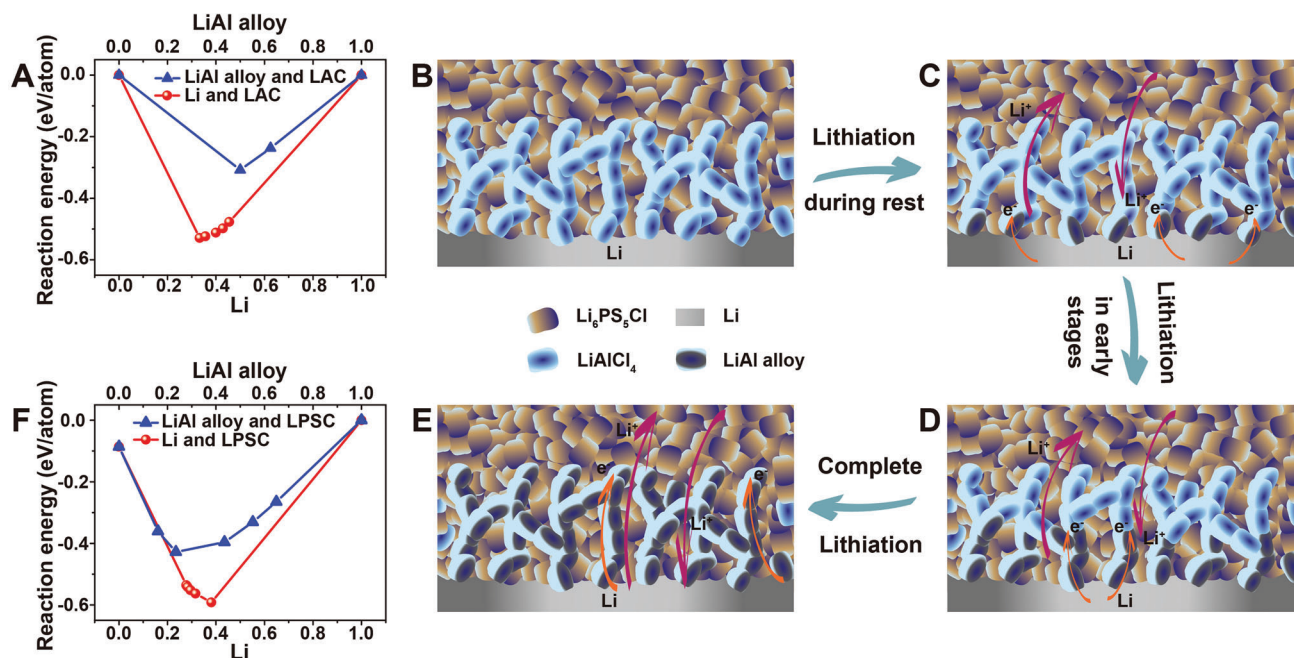


Figure 1. Theoretical calculations and schematic diagrams. A) Theoretical calculated reaction energy between Li metal, Li–Al alloy and LAC as a function of mixing ratio.^[11a] B–E) Schematic diagram: Halide electrolyte gradually reacts with Li metal to complete the lithiation process during the rest process. F) Theoretical calculations demonstrate reduced reaction energy between LPSC and Li–Al alloy as a function of the mixing ratio.^[11a]

electrochemical stability window, and good compatibility with oxide cathodes.^[9] Their main drawback is their instability against Li metal anode. The metal halide SEs chemically react with Li metal to form Li–M alloy (M represents another metal except for Li) and LiCl, thus prohibiting their direct contact with Li metal.^[9f,10] Metal halides are often used as a catholyte, not an anolyte. With reverse thinking, the product Li–M alloy is a good electron conductor, which can act as a suitable Li deposition carrier and a dendrite “inhibitor”. Therefore, halide SEs are an excellent choice for in situ constructing 3D Li metal anode for high-performance ASSLMBs.

Here, we rationally utilize the chemical reaction characteristics between metal halides and Li metal to in situ construct a 3D Li metal anode in ASSLMBs, which shows an enlarged solid-solid contact area and a continuous Li⁺ transport channel. First, sulfide and halide electrolytes are mixed uniformly and used as a sacrificial layer (SL) on the anode side. When the SL contacts the Li metal anode, halides would be lithiated gradually by their continued reactions with the Li metal anode. As a result, the 3D Li metal anode can be in situ formed. The in situ formed Li alloy acts as a lithiophilic substrate, which reduces Li nucleation overpotentials and uniform Li deposition. In addition, this method also mitigates the side reaction between sulfides and Li metal because of the smaller potential difference between sulfides and alloy than that between sulfides and Li metal. The halides that are separated by sulfides do not react with Li metal, which will act as the electrolytes to conduct Li⁺ in the battery. The sulfide SEs in the SL form continually Li⁺ transport pathways, preventing dead Li formation during the Li stripping process. Moreover, the stereoscopic structures of the in situ formed 3D Li anode features high active specific surface areas, which can reduce local current

density and facilitate rapid Li⁺ flux and homogeneous Li deposition. Additionally, the cracking in solid electrolyte and interfacial void formation problems have been significantly mitigated. As a result, this in situ formed 3D Li metal anode realizes stable cycling all-solid-state Li metal batteries at high current densities and large capacities. The symmetric battery can be stable during cycling for >500 h at a high current density of 3 mA cm⁻² with large cycling capacities of 3 mA h cm⁻². Moreover, after long-term cycling, the Li metal anode keeps a flat surface without Li dendrites. All-solid-state batteries using 3D Li metal demonstrate excellent electrochemical performance. This strategy is simple, effective, and applicable to other solid-state battery systems.

2. Results and Discussion

In this work, we chose Li₆PS₅Cl (LPSC) as the Li⁺ conductor due to its high ionic conductivity, low grain boundary resistance, and relatively good stability with Li metal. Cost-effective LiAlCl₄ (LAC) is selected as the halide SEs in the SL to react with Li metal to generate Li–Al alloy (Figure 1A),^[11] because Al is the most abundant metal in the Earth’s crust.^[12] In addition, the formed Li–Al alloy has the following advantages. First, Li–Al alloy is often used as an interface modification in both liquid and solid batteries to accommodate Li⁺ deposition for Li metal anodes.^[13] Besides, Li–Al alloy shows good chemical compatibility with sulfide SEs.^[14] Second, the Li–Al alloy anode has a moderate gravimetric capacity, which is preferred in this design because it will consume less Li metal to form Li–Al alloy. Moreover, Li–Al alloy exhibits minor volume change and the composition variation of Li–Al alloy during the alloying process is in a very narrow range, which is beneficial to forming a stable anode.^[15]

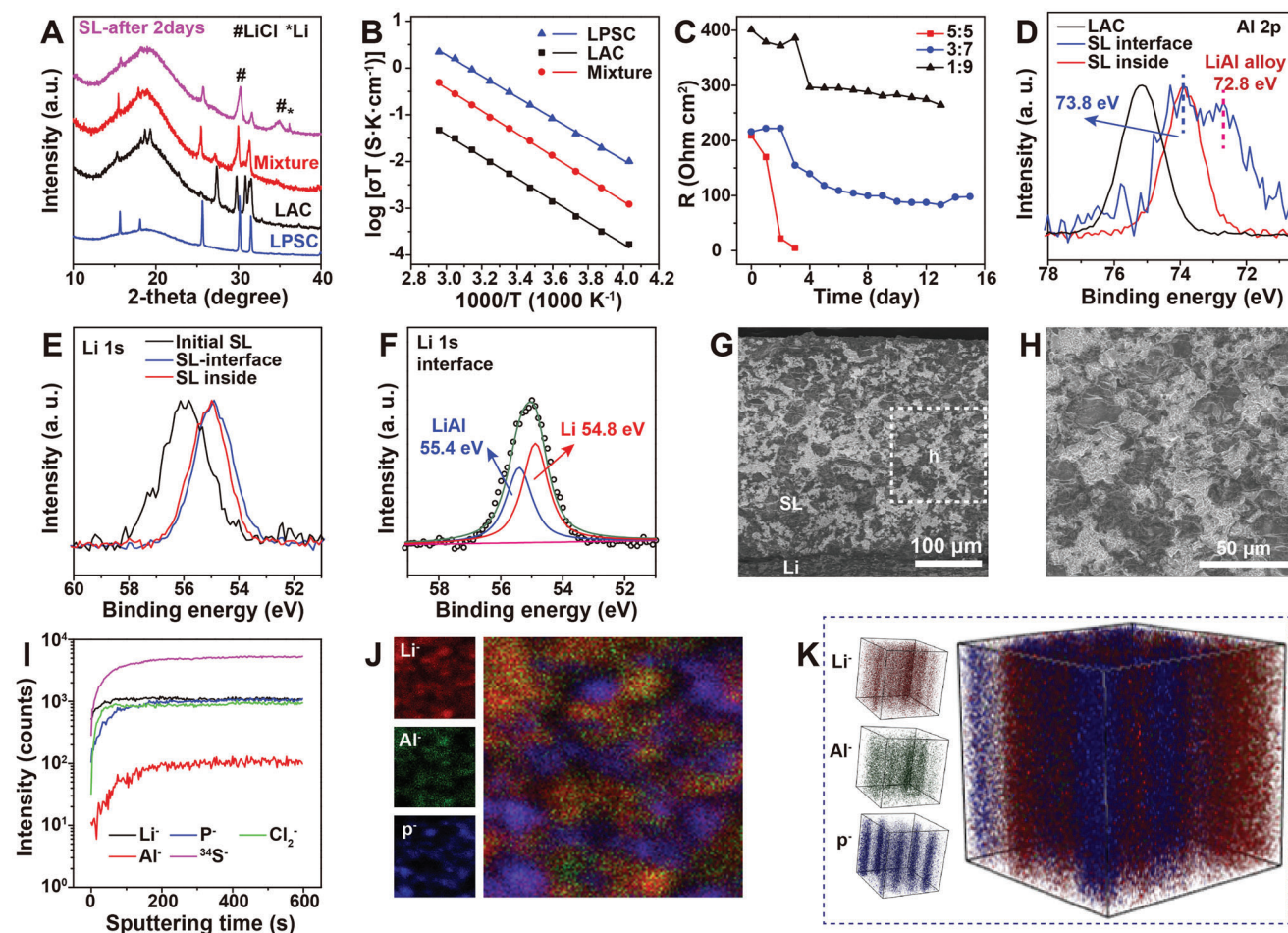


Figure 2. Properties, structures, and lithiation behaviors of the SL. A) XRD of LAC, LPSC, SL, and the SL after 2 days contacting with Li metal. B) Arrhenius plots of LAC, LPSC, and SL conductivities at elevated temperatures. C) EIS evolution of the Li/SL/Li battery with the LAC and LPSC mass ratio of 1:9, 3:7, and 1:1 during the rest time. High-resolution XPS D) Al 2p, E) Li 1s, and F) fitted Li 1s spectra of SL before and after lithiation. G, H) SEM images of the SL in the Li/SL-50wt.%/Li battery of (C) after rest for 2 days. I) TOF-SIMS depth profiles of various secondary ion species, J) ToF-SIMS images, and K) 3D reconstruction of the Li^+ , Al^+ , and P^+ secondary ion species based on the depth profiles obtained from the inside part of SL in the Li/SL-50wt.%/Li battery after rest for 2 days. (Sputter speed: 0.07 nm s^{-1} , sputter area: $128 \times 128 \mu\text{m}^2$).

The mechanism of the lithiation process is as follows. First, LAC halide and LPSC sulfide are mixed by ball milling to acquire a uniform mixture, which is placed on the anode side as a SL during the battery assembly. In the SL, the halides directly in contact with Li metal spontaneously react with Li metal to form a Li–Al alloy. Li–Al alloys can further react with the contacted LAC based on their thermal dynamics (Figure 1A). Second, the potential difference between Li metal and Li–Al alloy further leads to lithiation until the potential of alloy is similar with that of Li metal. The in situ formed alloy acts as an electron conductor in the 3D structure, while the sulfide in the SL serves as a Li^+ conductor to form a continuous 3D Li^+ transport pathway. Based on those two steps, a 3D Li metal anode is in situ formed in ASSLMs. There are four merits of the in situ formed 3D Li metal anodes. First, the sulfide and the insulative LiCl formed by the conversion reaction act as a structural buffer layer, effectively suppressing the considerable volume change of the anode at large current densities. Second, the in situ formed 3D Li metal anode can mitigate the instability between Li metal and sulfide because of the reduced potential

difference and good chemical compatibility between Li–Al alloy and sulfide SEs.^[14] Third, the in situ formed 3D Li metal anode can uniform electron and Li^+ distribution, reduce local current density, and accommodate Li deposition. Fourth, the Li–Al alloy provides multitudinous lithiophilic sites, which can reduce the nucleation overpotential of Li effectively and regulate Li deposition behavior, thus inhibiting the initiation of Li dendrite growth. This strategy is equivalent to converting a part of the electrolyte into a part of the anode, and the thickness of the electrolyte is therefore reduced, thence no compromise in energy density.

As a proof of concept, LPSC and LAC were synthesized as described in Supporting Information. The X-ray powder diffraction (XRD) patterns of LAC, LPSC, and their mixture are shown in Figure 2A. The XRD signal of the mixture combines the XRD characteristics of both LAC and LPSC. The ionic transport properties of LAC, LPSC, and their mixture with a mass ratio of 1:1 were analyzed by temperature-dependent electrochemical impedance spectroscopy (EIS) (Figure S1A–C, Supporting Information). The corresponding Arrhenius plots are displayed in

Figure 2B. LAC, LPSC, and their mixture showed ionic conductivities of 1.8×10^{-5} , 1×10^{-3} , and 1.7×10^{-4} S cm $^{-1}$ at 25 °C, respectively, with an activation energy of 0.46, 0.44, and 0.47 eV, respectively.

To construct continuous 3D Li $^{+}$ and electron transport pathways, the appropriate ratio of LAC in the SL should be determined. For this purpose, three types of SL with the LAC mass ratios of 10%, 30%, and 50% were prepared, and the Li/SL-10wt.%/Li, Li/SL-30wt.%/Li, and Li/SL-50wt.%/Li symmetric batteries were assembled. Since the alloying reactions between LAC and Li metal are thermodynamically spontaneous (Figure 1A) and occur during the standing process, the influence of the rest time on the alloying reaction degree is investigated first. By monitoring the EIS evolution during the rest time (Figure S2, Supporting Information), it is found that the resistance of the Li/SL/Li symmetric batteries decreases, implying the continuous reactions between Li metal and LAC. More interestingly, the Li/SL-50wt.%/Li battery shows short circuit after 2 days (Figure 2C; Figure S2, Supporting Information), indicating that the SL with 50 wt.% LAC reacts quickly with Li metal to form the connected electronic and ionic pathways. The whole SL in Li/SL-50wt.%/Li battery turns black after 2 days of rest (Figure S3A, Supporting Information). Furthermore, XRD peaks of LAC disappear and LiCl characteristic peaks shows up (Figure 2A), suggesting sufficient reactions between Li metal and LAC. Besides, X-ray photoelectron spectroscopy (XPS) was carried out to analyze the chemical information of this in situ formed 3D Li metal anode (Figure 2D–F). Compared with pristine LAC, the Al 2p spectrum of the SL interface reveals the significant signal of Li–Al alloy (72.8 eV)^[16] and other compositions of Li–Al alloy (73.8 eV, between LAC and Li–Al alloy), confirming the formation of Li–Al alloys after 2 days. Furthermore, the inner of the SL also illustrates an Al 2p peak at 73.8 eV, demonstrating that the alloying reaction diffuses to the inside of the SL (Figure 2D). Accordingly, the Li 1s spectrum of the interface and inner of the SL shows different bond energy than the initial SL (LAC mix with LPSC) (Figure 2E). Li–Al alloy is discernible at 55.4 eV (Figure 2F).^[17] These XPS results illustrate that almost all the LAC in SL is converted into Li–Al alloy and LiCl, consistent with the thermodynamic predictions (Table S1, Supporting Information). The S 2p and P 2p spectra of both the LPSC and the in situ formed 3D Li metal anode were found to be similar, suggesting that the structure of the LPSC remains stable during the formation process of the anode (Figure S4, Supporting Information). This observation is in line with the results obtained from XRD analysis (Figure 2A).

Figures 2G,H show the scanning electron microscopy (SEM) cross-sectional images of SL after lithiation, which display two kinds of species with different brightness that reflects their different electronic conductivity (Figures S3B and S3C, Supporting Information). The black species is Li–Al alloy because of its high electronic conductivity while the bright species represent the LPSC electrolyte because of its low electronic conductivity. They are closely connected in horizontal and vertical directions, constructing percolating ionic and electronic pathways, which are desirable for the 3D anode. Furthermore, time-of-flight secondary ion mass spectrometry (TOF-SIMS) was employed to detect the composition distribution of the lithiated SL. Figure 2I shows the depth profiles of various secondary ion species. With increasing depth, the intensity of the Li $^{+}$, Al $^{+}$, Cl $_{2}^{-}$, P $^{-}$, and 34 S $^{-}$

species are saturated after 100 s sputtering time, indicating the uniform distribution of these species inside the lithiated SL. Interestingly, the TOF-SIMS images (Figure 2J) and 3D reconstruction of total ions (Figure 2K) of the lithiated SL display a 3D interweaving structure, which further confirms that the 3D ion and electron conduction pathways are successfully constructed inside the SL. Hence, the SL with 50 wt.% LAC has been selected to in situ construct a 3D Li anode for all-solid-state batteries in the following parts.

To analyze this complicated reaction process and interfacial evolution during the rest time, in situ EIS were carried out and further resolved by distribution of relaxation times (DRT). DRT is a model-free method, which can separate the highly coincident physical and chemical processes in this complex system by converting the EIS from frequency to time constant.^[18] Obviously, the semicircle in middle-low frequency evolved from emerging to completely disappearing in the in situ EIS spectra (Figure 3A), which may originate from the emergence and completion of the reaction between Li metal and LAC. Four different specialized relaxation times can be distinguished in the DRT results, which are located at 10^{-7} , 10^{-5} , 10^{-5} to 10^{-4} , and 10^{-1} to 1 and are labeled as τ_1 , τ_2 , τ_3 , and τ_4 . The τ_1 at the ultrahigh frequency and time constant of 10^{-7} s represents the feature of grain boundary response of SEs (Figure 3B). The intensity of this peak continuously decreases and then stabilizes after rest for 18 h (Figure 3C). The peak areas in DRT represent the impedance value of the specialized electrochemical process. This phenomenon can be ascribed to the increased and then stabilized specific surface area during the reaction process between Li metal and LAC, thereby lowering area resistance. The stabilizing of this peak indicates the completed reaction and the successful buildup of 3D Li anode. Furthermore, the fading of τ_2 and τ_3 demonstrates the continuous reaction between Li metal and SL, representing the diverse interfacial transition of Li, alloy, electrolytes, and some medium products during this reaction process. The disappearance of these special peaks after rest for 18 h indicates the completed reaction between Li metal and SL. The emergence of τ_2 and τ_3 was also accompanied by the appearance of new peaks of τ_4 . The specific R_{ct} at τ_4 represents the emergence of alloy/SEs interfaces.^[18] To explore whether the initial electrochemical process has an impact on the interfacial reaction processes, Li/SL/LPSC/SL/Li batteries were subjected to direct charging-discharging without an initial rest process, at a current density of 0.5 mA cm $^{-2}$ (Figure S5A–C, Supporting Information). The in situ EIS and DRT results revealed that the interfacial evolution process in the batteries without rest was similar to that with a rest process, suggesting that the initial electrochemical process does not affect the interfacial reaction process.

In addition, to investigate whether soft-short circuit and the further interface evolution occur in the stabilized 3D Li metal anode, the symmetric battery was monitored by in situ EIS and analyzed by DRT during cycling at different current densities and capacities (Figure 3D–F; Figure S6, Supporting Information). The symmetric battery was plating/stripping for 1 h at 0.5, 1, 1.5, 2, and 3 mA cm $^{-2}$. According to the DRT results, the intensity of τ_1 keeps relatively stable, indicating a stable anode. Specifically, the emergence of two new processes of τ_5 (at 1 to 10 s) and τ_6 (at $\approx 10^{-6}$ s) represent the plating/stripping of Li metal and the emerging of SEI in the battery (Figure 3E,F), respectively.^[18] The

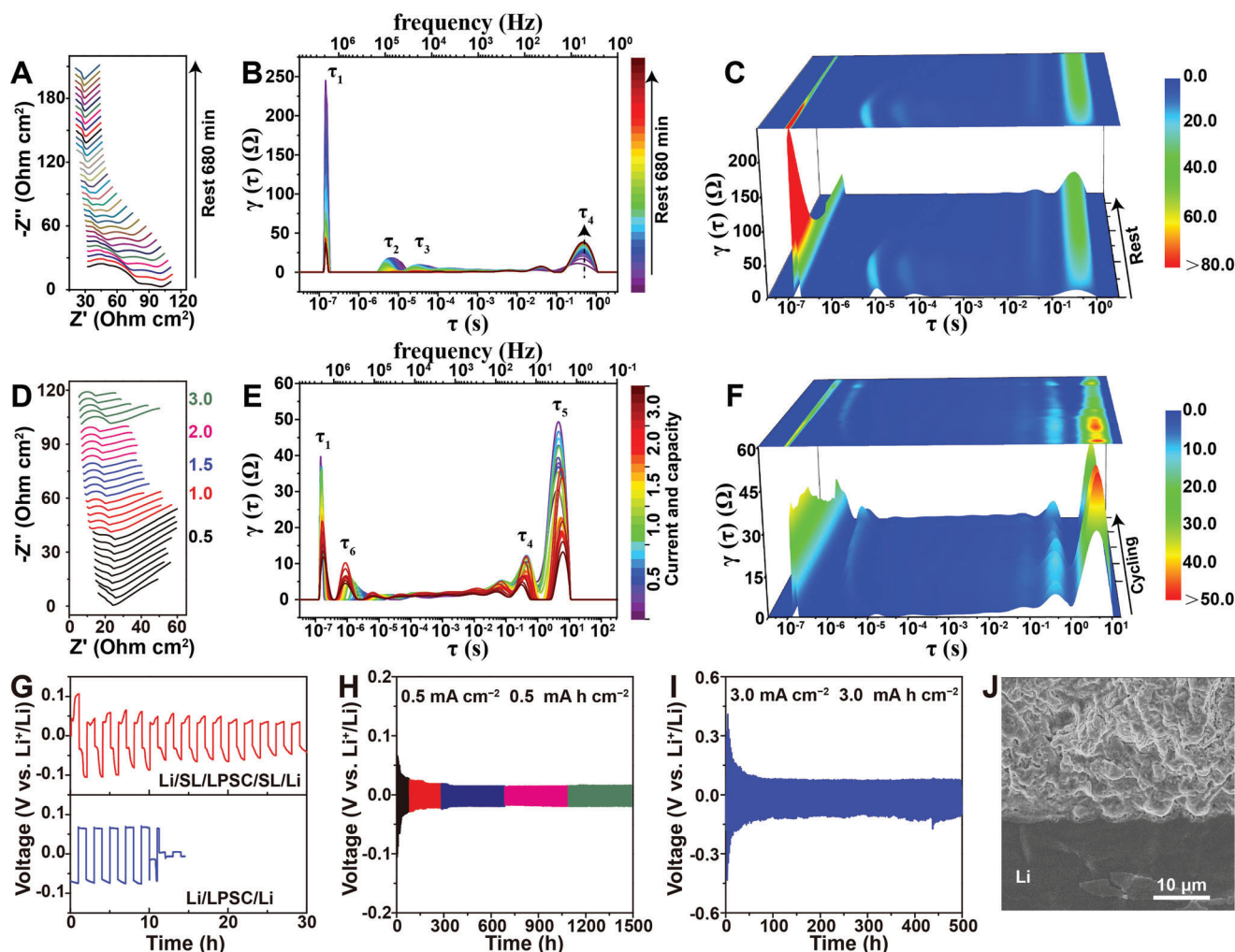


Figure 3. Electrochemical performance and morphologies of the symmetric batteries. EIS evolution and corresponding DRT transformation of the Li/SL/LPSC/SL/Li batteries during A–C) the initial rest process, and D–F) cycling at different current densities. G) The initial voltage profile of Li/SL/LPSC/SL/Li (up, red line) and Li/LPSC/Li (down, blue line) batteries at 0.5 mA cm^{-2} for 0.5 mA h cm^{-2} . Voltage profiles of Li/SL/LPSC/SL/Li symmetric batteries cycling H) at 0.5 mA cm^{-2} for 0.5 mA h cm^{-2} with EIS detection after certain cycles and I) at 3.0 mA cm^{-2} for 3.0 mA h cm^{-2} , respectively. J) SEM image of LPSC-SL-Li anode after long-term cycle.

existence of the special process of Li deposition indicates that there is no soft-short circuit in this process, which also reflects that DRT is an effective method for soft-short diagnosis in the battery. DRT analysis suggests that the in situ formed 3D Li metal anode results in the relatively uniform Li^+ flux in all-solid-state batteries under high current density and deposition capacities.

Figure 3G compares the cycling stability of Li/LPSC/Li and Li/SL/LPSC/SL/Li symmetric batteries under a current density of 0.5 mA cm^{-2} and deposition capacity of 0.5 mA h cm^{-2} . Without interfacial SL, short circuits occur at 20 h. With the SL, Li/SL/LPSC/SL/Li symmetric batteries demonstrate ultra-stable cycling stability for 1500 h after the initial interfacial stabilization process (initial 8 cycles) (Figure 3G,H), demonstrating that the SL help to form a stable Li/electrolyte interface and effectively suppresses Li dendrite growth. After long-term cycling, Li deposition resistance is gradually reduced, as verified by EIS and DRT analysis (Figure S7, Supporting Information). Moreover, when the current density and areal capacity increase to 3 and 3 mA h cm^{-2} , the

symmetric battery demonstrates an ultra-stable performance for 500 h (Figure 3I).

To observe the Li deposition morphology and visualize the in situ formed 3D Li metal anode, the symmetric batteries were disassembled after long-term cycling and ex-situ SEM and SEM energy dispersive X-ray spectrometry (SEM-EDS) mapping were carried out to characterize the cross-section of the Li/SL interface. The thickness of the SL is $\approx 63 \mu\text{m}$ (Figure S8A,B, Supporting Information). Obviously, the Li metal anode maintains intimate contact with the SL according to the cross-section of Li/SL/sulfide. And both the Li metal anode and SL keep compact and dense stacking (Figure 3J; Figure S8 and S9, Supporting Information). Notably, the Al and S element mappings indicate the structure and position of the in situ formed 3D anode remained stable and steady during the repeat plating/stripping process (Figure S8B,D, Supporting Information). In addition, the in situ formed 3D anode enables homogeneous Li^+ flux distribution and uniform mass transport at high current density.^[19] The

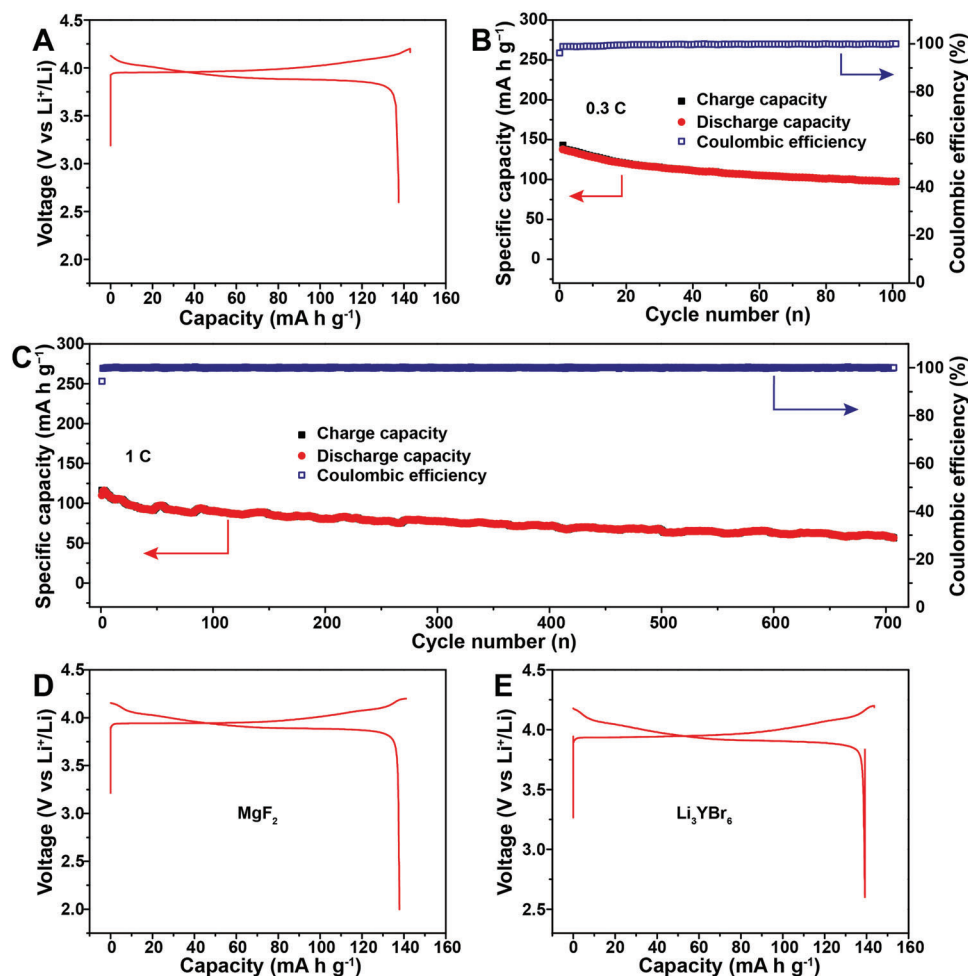


Figure 4. Electrochemical performance and universality of this method. A) The initial galvanostatic charge/discharge voltage profiles, and B,C) long-term cycling performance of the Li/SL/LPSC/LIC/LCO full battery rest for 2 days. Galvanostatic charge/discharge voltage profiles of the full batteries rest for 2 days with D) MgF_2 , and E) Li_3YBr_6 as the reactor in the SL, respectively.

lithiophilic Li–Al alloy has a good metallic Li affinity can effectively reduce the nucleation overpotential of Li and guide the Li deposition, which leads to even Li nucleation and deposition.^[20] Moreover, the maintained sulfide and the reaction product LiCl act as a structural buffer layer, effectively alleviate volume expansion of the anode. Accordingly, the good conformal contact between Li and the solid electrolyte is maintained even after cycling for 1500 h at high current densities and capacities. This result indicates that the in situ formed 3D Li metal anode can effectively improve the Li deposition/dissolution behaviors.

Furthermore, ASSLMs with a configuration of Li/SL/LPSC/LIC/LCO were assembled to demonstrate the practical application of the in situ formed 3D Li metal anode. In order to acquire a stable anode in the full battery, we prolong the rest time to 2 days (Figure S10, Supporting Information), a direct plateau at 3.9 V without an additional platform is observed in the initial galvanostatic charge/discharge voltage profiles (Figure 4A). This phenomenon indicates that the alloying process is complete during the standing process and a Li-rich alloy anode is formed. Therefore, after the alloy forms, the anode remains stable and acts as a Li metal anode behavior. In addition, the in situ formed

3D Li anode enables homogeneous Li^+ flux distribution and uniform mass transfers at high current density that can induce even Li nucleation and deposition.^[13,21] As a result, the assembled battery shows a high initial discharge capacity of $137.5 \text{ mA h g}^{-1}$, and a high initial Coulombic efficiency (CE) of 96% (Figure 4A). More impressively, the battery provides stable cycling for >100 cycles at 0.3C-rate and with a capacity retention of 71% (Figure 4B). When the current density was increased to 1C-rate, the battery also shows a high discharge capacity of 115 mA h g^{-1} , and can stably cycle for >700 cycles (Figure 4C). However, the electrochemical performance of the Li/LPSC/LIC/LCO battery exhibit poor stability and increased polarization as cycling. Moreover, there is a significant dendrite growth-induced short circuit phenomenon (Figure S11, Supporting Information). These results indicate that the in situ formed 3D Li metal anode can be used in the all-solid-state battery to achieve good electrochemical performance. This straightforward and easy to implement strategy has great potential for widespread use in practical applications. To prove the generality of this concept, other salts, halides, and sulfides that can react with Li metal can also be used in this strategy. Several typical materials, such as non-ionic conductor (i.e., MgI_2 , and MgF_2) and

ionic conductor (i.e., Li_3HoCl_6 , Li_3YBr_6 , and $\text{Li}_{10}\text{GeP}_2\text{S}_{12}$) materials have been attempted and unanimously demonstrated excellent charge-discharge curves with negligible polarization and high CE (>92%) (Figure 4D,E; Figure S12, Supporting Information). These results show that the strategy of in situ constructing 3D Li metal anodes is universal and applicable in the solid-state battery systems.

3. Conclusion

In summary, we proposed a reverse train of thought strategy to construct the 3D Li for all-solid-state Li metal batteries (ASSLMBs) by rationally utilizing the spontaneous chemical reactions between halides and Li metal. By introducing a sulfide and halide mixture at the anode side to serve as a sacrificial layer (SL), the reaction product Li–Al alloy and well-maintained $\text{Li}_6\text{PS}_5\text{Cl}$ in situ form continuous electronic and Li^+ pathways, respectively. The detailed evolution process of this 3D anode in $\text{Li}|\text{Li}|$ symmetric batteries was analyzed by in situ EIS and DRT. This in situ formed 3D Li metal anode possesses a high surface area to accommodate Li^+ deposition for Li metal anodes by reducing local current density. In addition, the in situ formed lithiophilic Li–Al alloy is vital to homogeneous Li^+ flux distribution and uniform mass transfers at high current densities, which promote even Li nucleation and deposition. As a result, all-solid-state $\text{Li}|\text{Li}|$ symmetric batteries demonstrate stable cycling with a high capacity of 3 mA h cm^{-2} and a high current density of 3 mA cm^{-2} for 500 h. Coupled with LiCoO_2 , ASSLMBs present stable cycling for over 700 cycles. Moreover, the generality of this strategy makes this method more practical. This work breaks off the traditional concept of the anode design in all-solid-state batteries and other solid systems to promote a high-performance and easy to implement strategy for 3D Li for ASSLMBs.

4. Experimental Section

Preparation of the Mixture: LiCl (Sigma–Aldrich) and AlCl_3 (Sigma–Aldrich) were ground together in the ratio corresponding to the stoichiometry of LiAlCl_4 (LAC). 1 g of powder was then loaded into a ZrO_2 ball-mill jar with 40 g ZrO_2 balls and ball-milled at 500 rpm. for 10 h. $\text{Li}_6\text{PS}_5\text{Cl}$ (LPSCl) was received from China Automotive Battery Research Institute Co., Ltd. The mixtures were prepared by mixing LAC and LPSC with a certain mass ratio. Corresponding weights of LAC and LPSC were loaded into a ZrO_2 ball-mill jar with 40 g ZrO_2 balls and ball-milled at 100 rpm. for 2 h. The mixtures that use the MgI_2 , Li_3HoCl_6 , Li_3YBr_6 , and $\text{Li}_{10}\text{GeP}_2\text{S}_{12}$ as the reactor in the SL, respectively, were prepared with the same method as using LAC with the mass ratio of 50%.

Characterizations: The X-ray diffraction (XRD) patterns were carried out using a Bruker AXS D8 Advance with $\text{Cu K}\alpha$ X-ray radiation ($\lambda = 1.54178\text{ \AA}$). Kapton tape was used to seal the powder from the air. Patterns were collected from 10° to 80° (2θ) using a step size of 2° min^{-1} at room temperature. Scanning electron microscopy (SEM) images were obtained using a Hitachi S-4800 field emission SEM equipped with energy dispersive spectroscopy (EDS). The X-ray photoelectron spectroscopy (XPS) data were recorded with a monochromatic $\text{Al K}\alpha$ source using a Thermo Scientific K-Alpha Spectrometer. The time-of-flight secondary ion mass spectrometry (TOF-SIMS) measurements were performed on a TOF-SIMS IV (ION-TOF GmbH, Germany) with a 25 keV bismuth liquid metal ion source with a base pressure at $\approx 10^{-8}$ mbar in the analysis chamber. All spectra were collected in negative secondary ion mode. The measurement

area was set to $128 \times 128\text{ }\mu\text{m}^2$. Depth profiles were obtained by sputtering ion beams of Cs^+ (3 keV).

Ionic Conductivity and Activation Energy Measurements: Ionic conductivity was measured by electrochemical impedance spectroscopy (EIS) at temperatures ranging from -25 to 65°C using a VMP3 potentiostat/galvanostat (Bio-logic) in the frequency range from 7 MHz to 1 Hz and the voltage amplitude is 10 mV. 100 mg of the solid electrolyte powder was cold-pressed into a pellet at 3 tons in a 10 mm diameter die. Then, ketjen black was added and served as blocking electrodes for EIS measurements.

The activation energy (E_a) is calculated using the equation

$$\sigma T = \sigma_0 \exp(-E_a/k_B T) \quad (1)$$

where σ is ionic conductivity, σ_0 is the Arrhenius prefactor, T is absolute temperature, E_a is the activation energy, and k_B is the Boltzmann constant.

Electrochemical Characterizations $\text{Li}|\text{Li}|$ Symmetric Batteries: To keep the same total LAC content in each $\text{Li}/\text{SL}/\text{Li}$ battery, the weights of the mixtures with 10 wt.%, 30 wt.%, and 50 wt.% LAC are 400, 133.4, and 80 mg, respectively. The powders were pressed by 4 tons (T) in a 10 mm diameter die. Then, two pieces of bare Li metal were placed onto both sides of the pellet to form the $\text{Li}/\text{SL}/\text{Li}$ symmetric batteries.

Eighty milligrams of LPSC was pressed by 4 T in a 10 mm diameter die. Then, two pieces of bare Li metal were placed onto both sides of the pellet to form the $\text{Li}/\text{LPSC}/\text{Li}$ symmetric batteries. For the assembly of $\text{Li}/\text{sacrificial layer (SL)}/\text{LPSC}/\text{SL}/\text{Li}$ symmetric batteries, 80 mg LPSC was pressed by 2 T in a 10 mm diameter die. Then 10 mg of LAC and LPSC mixture was spread uniformly on both sides of the pellet to serve as the SL and pressed by 4 T, afterward, two pieces of bare Li metal were placed onto both sides of the pellet to form the $\text{Li}/\text{SL}/\text{LPSC}/\text{SL}/\text{Li}$ symmetric batteries.

All-Solid-State Battery Fabrication: LIC was synthesized following our previously reported procedure. Cathode composites were prepared via uniformly mixing commercial LiCoO_2 (LCO) and Li_3InCl_6 (LIC) with a mass ratio of 7:3 using a roll mixer. First, 80 mg of LIC was compressed at 2 T (10 mm diameter), and then 40 mg of LPSC was spread over one side of the LIC pellet and pressed at 2 T. Afterward, 10 mg of the mixture of LAC and LPSC was spread over the surface of LPSC and pressed at 2 T. 10 mg of the composite cathode mixture was spread on the surface of LIC pellet and pressed at 3 T to serve as SL. Then, a piece of bare Li metal was attached to the surface of the SL. The cell was placed into a stainless steel casing with a constantly applied pressure of $\approx 1.5\text{ T}$. Galvanostatic cycling of the cell was carried out in the voltage range of 2.6–4.2 V versus Li^+/Li .

In Situ EIS Test: The EIS test was performed in different states of charge. A galvanostatic charge/discharge operation was performed on the battery. EIS measurements were conducted after every 1 h of charge/discharge, before and after that the cells were placed at rest for 1 h. The voltage range of the galvanostatic charge/discharge tests was 2–4.2 V, at a 0.07C rate. The frequency range of the EIS test was 7 MHz to 100 mHz, and the amplitude was 10 mV. DRT transformation was carried out with the free software DRTtools,^[18a] and all parameters are consistent in the calculation process to ensure the consistency of the DRT results.

Supporting Information

Supporting Information is available from the Wiley Online Library or from the author.

Acknowledgements

H.D., C.W., and R.Y. contributed equally to this work. H.D. and R.Y. appreciated the support of Mitacs through the Mitacs Accelerate program. C.W. acknowledges the Banting Postdoctoral Fellowship (BPF-180162). This work was supported by Natural Sciences and Engineering Research Council of Canada (NSERC), Canada Research Chair Program (CRC), Canada Foundation for Innovation (CFI), Ontario Research Fund (ORF), China Automotive Battery Research Institute Co., Ltd., Glabat Solid-State Battery Inc., and University of Western Ontario.

Conflict of Interest

The authors declare no conflict of interest.

Data Availability Statement

The data that support the findings of this study are available from the corresponding author upon reasonable request.

Keywords

electrochemical energy storage, all-solid-state batteries, sulfide electrolytes, 3D Li anodes, in situ construction

Received: March 16, 2023
Revised: April 10, 2023
Published online: May 11, 2023

- [1] a) A. Manthiram, X. Yu, S. Wang, *Nat. Rev. Mater.* **2017**, 2, 16103; b) J. Janek, W. G. Zeier, *Nat. Energy* **2016**, 1, 16141.
- [2] a) F. D. Han, A. S. Westover, J. Yue, X. L. Fan, F. Wang, M. F. Chi, D. N. Leonard, N. Dudney, H. Wang, C. S. Wang, *Nat. Energy* **2019**, 4, 187; b) X. Han, Y. Gong, K. Fu, X. He, G. T. Hitz, J. Dai, A. Pearse, B. Liu, H. Wang, G. Rubloff, Y. Mo, V. Thangadurai, E. D. Wachsmann, L. Hu, *Nat. Mater.* **2016**, 16, 572; c) Y. Lu, C.-Z. Zhao, J.-K. Hu, S. Sun, H. Yuan, Z.-H. Fu, X. Chen, J.-Q. Huang, M. Ouyang, Q. Zhang, *Sci. Adv.* **2022**, 8, eadd0510; d) Z. Ning, D. S. Jolly, G. Li, R. De Meyere, S. D. Pu, Y. Chen, J. Kasemchainan, J. Ihli, C. Gong, B. Liu, D. L. R. Melvin, A. Bonnin, O. Magdysyuk, P. Adamson, G. O. Hartley, C. W. Monroe, T. J. Marrow, P. G. Bruce, *Nat. Mater.* **2021**, 20, 1121.
- [3] C.-P. Yang, Y.-X. Yin, S.-F. Zhang, N.-W. Li, Y.-G. Guo, *Nat. Commun.* **2015**, 6, 8058.
- [4] a) H. Duan, W. P. Chen, M. Fan, W. P. Wang, L. Yu, S. J. Tan, X. Chen, Q. Zhang, S. Xin, L. J. Wan, Y. G. Guo, *Angew. Chem., Int. Ed.* **2020**, 59, 12069; b) J. Liang, X. Li, Y. Zhao, L. V. Goncharova, W. Li, K. R. Adair, M. N. Banis, Y. Hu, T.-K. Sham, H. Huang, L. Zhang, S. Zhao, S. Lu, R. Li, X. Sun, *Adv. Energy Mater.* **2019**, 9, 1902125; c) Y. Pang, J. Pan, J. Yang, S. Zheng, C. Wang, *Electrochem. Energy Rev.* **2021**, 4, 169.
- [5] C. Yang, L. Zhang, B. Liu, S. Xu, T. Hamann, D. McOwen, J. Dai, W. Luo, Y. Gong, E. D. Wachsmann, L. Hu, *Proc. Natl. Acad. Sci. U.S.A.* **2018**, 115, 3770.
- [6] L. Ye, X. Li, *Nature* **2021**, 593, 218.
- [7] a) H. Ye, S. Xin, Y.-X. Yin, Y.-G. Guo, *Adv. Energy Mater.* **2017**, 7, 1700530; b) Y. Liu, D. Lin, Z. Liang, J. Zhao, K. Yan, Y. Cui, *Nat. Commun.* **2016**, 7, 10992; c) W. Liu, D. Lin, A. Pei, Y. Cui, *J. Am. Chem. Soc.* **2016**, 138, 15443; d) H. Liang, L. Wang, L. Sheng, H. Xu, Y. Song, X. He, *Electrochem. Energy Rev.* **2022**, 5, 23.
- [8] a) W. D. Jung, M. Jeon, S. S. Shin, J.-S. Kim, H.-G. Jung, B.-K. Kim, J.-H. Lee, Y.-C. Chung, H. Kim, *ACS Omega* **2020**, 5, 26015; b) J. Ruhl, L. M. Riegger, M. Ghidui, W. G. Zeier, *Adv. Energy Sustainability Res.* **2021**, 2, 2000077.
- [9] a) J. Liang, X. Li, K. R. Adair, X. Sun, *Acc. Chem. Res.* **2021**, 54, 1023; b) K.-H. Park, K. Kaup, A. Assoud, Q. Zhang, X. Wu, L. F. Nazar, *ACS Energy Lett.* **2020**, 5, 533; c) X. Li, J. Liang, J. Luo, M. Norouzi Banis, C. Wang, W. Li, S. Deng, C. Yu, F. Zhao, Y. Hu, T.-K. Sham, L. Zhang, S. Zhao, S. Lu, H. Huang, R. Li, K. R. Adair, X. Sun, *Energy Environ. Sci.* **2019**, 12, 2665; d) X. Li, J. Liang, X. Yang, K. R. Adair, C. Wang, F. Zhao, X. Sun, *Energy Environ. Sci.* **2020**, 13, 1429; e) T. Asano, A. Sakai, S. Ouchi, M. Sakaida, A. Miyazaki, S. Hasegawa, *Adv. Mater.* **2018**, 30, 1803075; f) S. Wang, Q. Bai, A. M. Nolan, Y. S. Liu, S. Gong, Q. Sun, Y. F. Mo, *Angew. Chem., Int. Ed.* **2019**, 58, 8039.
- [10] L. M. Riegger, R. Schlem, J. Sann, W. G. Zeier, J. Janek, *Angew. Chem., Int. Ed.* **2021**, 60, 6718.
- [11] a) A. Jain, S. P. Ong, G. Hautier, W. Chen, W. D. Richards, S. Dacek, S. Cholia, D. Gunter, D. Skinner, G. Ceder, K. A. Persson, *APL Mater.* **2013**, 1, 011002; b) N. Flores-González, N. Minafra, G. Dewald, H. Reardon, R. I. Smith, S. Adams, W. G. Zeier, D. H. Gregory, *ACS Mater. Lett.* **2021**, 3, 652.
- [12] a) H. Kwak, D. Han, J. Lyoo, J. Park, S. H. Jung, Y. Han, G. Kwon, H. Kim, S.-T. Hong, K.-W. Nam, Y. S. Jung, *Adv. Energy Mater.* **2021**, 11, 2003190; b) K. Wang, Q. Ren, Z. Gu, C. Duan, J. Wang, F. Zhu, Y. Fu, J. Hao, J. Zhu, L. He, C.-W. Wang, Y. Lu, J. Ma, C. Ma, *Nat. Commun.* **2021**, 12, 4410; c) A. A. Yaroshevsky, *Geochem. Int.* **2006**, 44, 48.
- [13] H. Kim, J. T. Lee, D.-C. Lee, M. Oschatz, W. I. Cho, S. Kaskel, G. Yushin, *Electrochem. Commun.* **2013**, 36, 38.
- [14] H. Pan, M. Zhang, Z. Cheng, H. Jiang, J. Yang, P. Wang, P. He, H. Zhou, *Sci. Adv.* **2022**, 8, eabn4372.
- [15] X. Gu, J. Dong, C. Lai, *Eng. Rep.* **2021**, 3, e12339.
- [16] a) H. Zhong, Y. Wu, F. Ding, L. Sang, Y. Mai, *Electrochim. Acta* **2019**, 304, 255; b) F. J. Esposto, K. Griffiths, P. R. Norton, R. S. Timsit, *J. Vac. Sci. Technol. A* **1994**, 12, 3245.
- [17] S. Han, Z. Li, Y. Zhang, D. Lei, C. Wang, *Energy Storage Mater.* **2022**, 48, 384.
- [18] a) T. H. Wan, M. Saccoccio, C. Chen, F. Ciucci, *Electrochim. Acta* **2015**, 184, 483; b) Y. Lu, C.-Z. Zhao, J.-Q. Huang, Q. Zhang, *Joule* **2022**, 6, 1172; c) H. Q.-a. Wang, J. Li, I. Wei-heng, W. Juan, Z. Quan-chao, Z. Jiu-jun, *J. Electrochem.* **2020**, 26, 607; d) B. A. Boukamp, *J. Phys. Condens. Matter* **2020**, 2, 042001; e) X. Chen, L. Li, M. Liu, T. Huang, A. Yu, *J. Power Sources* **2021**, 496, 229867; f) Y. Lu, C.-Z. Zhao, R. Zhang, H. Yuan, L.-P. Hou, Z.-H. Fu, X. Chen, J.-Q. Huang, Q. Zhang, *Sci. Adv.* **2021**, 7, eabi5520.
- [19] J. Zhu, D. Cai, J. Li, X. Wang, X. Xia, C. Gu, J. Tu, *Energy Storage Mater.* **2022**, 49, 546.
- [20] a) K. Yan, Z. Lu, H.-W. Lee, F. Xiong, P.-C. Hsu, Y. Li, J. Zhao, S. Chu, Y. Cui, *Nat. Energy* **2016**, 1, 16010; b) C. Yang, Y. Yao, S. He, H. Xie, E. Hitz, L. Hu, *Adv. Mater.* **2017**, 29, 1702714.
- [21] a) H. Zhuang, P. Zhao, G. Li, Y. Xu, X. Jia, *J. Power Sources* **2020**, 455, 227977; b) H. Ye, Y.-X. Yin, S.-F. Zhang, Y. Shi, L. Liu, X.-X. Zeng, R. Wen, Y.-G. Guo, L.-J. Wan, *Nano Energy* **2017**, 36, 411; c) N. Kumagai, Y. Kikuchi, K. Tanno, F. Lantelme, M. Chemla, *J. Appl. Electrochem.* **1992**, 22, 728.